lubricants

MDPI

Article

Durable Low-Friction Graphite Coatings Enabled by a Polydopamine Adhesive Underlayer

Adedoyin Abe [1,2], Fernando Maia de Oliveira [3], Deborah Okyere [4], Mourad Benamara [3], Jingyi Chen [4], Yuriy I. Mazur [3] and Min Zou [1,2,*]

[1] Department of Mechanical Engineering, University of Arkansas, Fayetteville, AR 72701, USA; aaabe@uark.edu
[2] Center for Advanced Surface Engineering, University of Arkansas, Fayetteville, AR 72701, USA
[3] Institute for Nanoscience and Engineering, University of Arkansas, Fayetteville, AR 72701, USA; fmaiade@uark.edu (F.M.d.O.); mourad@uark.edu (M.B.); ymazur@uark.edu (Y.I.M.)
[4] Department of Chemistry and Biochemistry, University of Arkansas, Fayetteville, AR 72701, USA; dtokyere@uark.edu (D.O.); chenj@uark.edu (J.C.)
* Correspondence: mzou@uark.edu; Tel.: +1-(479)-575-6671; Fax: +1-(479)-575-6982

Abstract

This study investigates the tribological performance and wear mechanisms of graphite and polydopamine/graphite (PDA/graphite) coatings on stainless steel under dry sliding conditions. While graphite is widely used as a solid lubricant, its poor adhesion to metal substrates limits long-term durability. Incorporating an adhesion-promoting PDA underlayer significantly improved coating lifetime and wear resistance. Tribological testing revealed that PDA/graphite coatings maintained a coefficient of friction (COF) below 0.15 for over seven times longer than graphite-only coatings. High-resolution scanning electron microscopy, SEM, and profilometry showed that PDA improved coating adhesion and suppressed lateral debris transport, confining wear to a narrow zone. Surface and counterface analyses confirmed enhanced graphite retention and formation of cohesive transfer films. Raman spectroscopy indicated only modest changes in the D and G bands. X-ray Photoelectron Spectroscopy, XPS analysis, confirmed that coating failure correlated with the detection of Fe and Cr peaks and oxide formation. Together, these results demonstrate that PDA enhances interfacial adhesion and structural stability without compromising lubrication performance, offering a strategy to extend the durability of carbon-based solid lubricant systems for high-contact-pressure applications.

Keywords: graphite; polydopamine; solid lubricant; coating performance; transfer film; wear mechanism

check for updates

Received: 11 July 2025
Revised: 21 September 2025
Accepted: 29 September 2025
Published: 30 September 2025

Citation: Abe, A.; Maia de Oliveira, F.; Okyere, D.; Benamara, M.; Chen, J.; Mazur, Y.I.; Zou, M. Durable Low-Friction Graphite Coatings Enabled by a Polydopamine Adhesive Underlayer. *Lubricants* **2025**, *13*, 433. https://doi.org/10.3390/lubricants13100433

Copyright: © 2025 by the authors. Licensee MDPI, Basel, Switzerland. This article is an open access article distributed under the terms and conditions of the Creative Commons Attribution (CC BY) license (https://creativecommons.org/licenses/by/4.0/).

1. Introduction

Solid lubricants are essential in aerospace, manufacturing, space, automotive, and biomedical systems, where conventional liquid lubricants often fail due to temperature, vacuum, or contamination constraints. These dry-film lubricants form a protective barrier between sliding surfaces, minimizing direct metal-on-metal contact and reducing adhesive wear [1]. However, because such coatings are typically thin, their service life is inherently limited, making durability and wear resistance critical areas of research [2,3].

Among solid lubricants, materials such as molybdenum disulfide (MoS_2), polytetrafluoroethylene (PTFE), hexagonal boron nitride (h-BN), and graphite are well studied for their ability to reduce friction via shear mechanisms [4]. Graphite, like h-BN and MoS_2,

possesses a lamellar structure with weak van der Waals forces between its graphene layers, allowing for low interlayer shear strength and excellent lubricity. Graphite and h-BN have similar layered hexagonal lattice structures, with the latter often called 'white graphite'; however, h-BN is an electrical insulator [5,6]. Unlike MoS_2, which is prone to oxidation in air and performs best in vacuum environments, graphite maintains low friction under ambient conditions [7]. Furthermore, its high thermal and electrical conductivity makes graphite preferable in applications where the insulating nature of PTFE is a limitation [8].

Despite these advantages, graphite is most commonly employed as a lubricant additive rather than as a standalone coating. It is frequently incorporated into polymers, metal matrices, lubricating oils, and ceramics to reduce friction and wear in composite systems [9–14]. As a dry-film coating, graphite is used in applications such as forming and stamping dies, as well as in components like bearings, seals, pump and valve parts, piston skirts, and motor brushes [1]. However, its standalone coating application [15] remains limited due to poor adhesion to substrates and weak cohesion between graphite flakes. Unlike viscoelastic PTFE, which forms continuous films, graphite coatings consist of discrete platelets that tend to delaminate or wear away quickly. Various strategies have been explored to improve cohesion and adhesion, including the use of epoxy binders and mechanical interlocking with roughened substrates [16–18]. Well-adhered graphite coatings have been shown to exhibit enhanced wear resistance. Given that steel accounts for over 85% of global metal usage [19], it remains a common and relevant substrate for graphite-based coatings in industrial applications.

Our previous findings [20] also demonstrated that polydopamine (PDA) improved the scratch resistance of graphite coatings, even under contact pressures exceeding 1.6 GPa. PDA is a bioinspired polymer known for its strong adhesion and surface functionalization capabilities. It has been used alone or in conjunction with traditional silanes to enhance coating-substrate bonding [21]. Its primary role is as an interfacial adhesive that improves coating retention in composite systems. For example, incorporating PDA beneath PTFE coatings has been shown to significantly improve durability during tribological testing [22]. Our prior study found that PDA increases the scratch resistance of graphite coatings by strengthening adhesion at the steel interface. On metallic and oxide surfaces, PDA binds primarily through coordination or chelating interactions between catechol groups and metal ions, which are facilitated by hydroxylated surface layers [23,24]. On carbon-based surfaces such as graphite, PDA interacts through π–π stacking between its aromatic moieties and graphitic basal planes, supplemented by hydrogen bonding [21,23,25,26]. These complementary interactions allow PDA to form conformal coatings on both organic and inorganic materials, making it an attractive candidate for adhesion enhancement in graphite-based tribological coatings.

While PDA has been widely explored for surface functionalization, its use as an adhesive underlayer to promote flake anchoring and tribofilm stability in graphite coatings remains underexplored. Moreover, the long-term performance of PDA-modified graphite coatings, particularly under reciprocating sliding conditions, has yet to be systematically investigated [13,18].

Many tribological systems experience repeated reciprocating motion, which imposes extended mechanical cycling and cumulative wear on solid lubricant coatings. In such scenarios, failure is governed not only by initial adhesion but also by the coating's ability to maintain structural and functional integrity over time. A key factor influencing long-term performance is the formation and stability of transfer films—thin lubricating layers that develop and persist on the counterface during sliding [8]. These films reduce interfacial shear stress, mitigate abrasive wear, and can significantly extend coating lifespan [27]. Despite their importance, the mechanisms of transfer film formation and retention in

dry-sliding PDA/graphite systems remain insufficiently understood, particularly under conditions simulating prolonged mechanical operation. Most prior studies have focused on small-scale, short-duration tests or bulk wear metrics of graphite, offering limited insight into the dynamic evolution of these films [28–31].

To address these gaps, the present study investigates the time-resolved wear behavior of graphite and PDA/graphite coatings under dry reciprocating sliding. We examine coating retention, coefficient of friction (COF), and the formation and evolution of transfer films at short-term (2-cycle), intermediate (1 h), and long-term (failure) sliding intervals. We hypothesize that PDA enhances both coating adhesion and transfer film stability, thereby improving wear resistance and extending graphite coating lifespan.

2. Materials and Methods

2.1. Materials

Polymerization of dopamine began with 0.03 g of dopamine hydrochloride (Sigma Aldrich, St. Louis, MO, USA, >98% purity) in 20 mL deionized water (DI water), along with 0.018 g of tris buffer (Sigma Aldrich) to create an alkaline environment for the reaction. 316 stainless steel (SS) substrates (McMaster-Carr, Elmhurst, IL, USA) used in this study were mirror finished sheet metal which was laser cut into 1″ SS squares (25.4 mm × 25.4 mm × 0.7 mm). The substrates were cleaned with acetone and wiped dry with lint-free laboratory wipes (KimTech, Kimberly-Clark, Irving, TX, USA). Graphite coatings were prepared using a water-based graphite suspension (AMLube 1127, AML industries, Warren, OH, USA) containing 25 vol.% graphite solids.

2.2. Sample Preparation

Graphite dispersions were prepared for dip coating by first ball-milling the commercial graphite suspension and then filtering it through a 40 μm mesh. This two-step process was employed to break up large agglomerates and improve particle dispersion prior to application. To assess the impact of ball milling and filtering on particle size, dynamic light scattering (DLS) measurements (Brookhaven ZetaPALS, Upton, NY, USA) were performed on the processed dispersions after 4000× dilution in deionized (DI) water. To ensure accurate DLS measurements, UV–Vis spectroscopy was first used to verify that sample absorbance remained within the instrument's linear range (0.1–1.0 AU), thereby minimizing deviations due to multiple scattering or absorbance saturation effects. This step ensured that DLS measurements would yield reliable hydrodynamic size distributions. The dispersions were diluted stepwise, and UV–Vis spectra were collected until the absorbance fell within this range, after which DLS measurements were conducted. Although these measurements reflect the behavior of diluted dispersions rather than the undiluted coating solution, they provide valuable insight into how each processing step influences dispersion properties.

For each condition, five DLS measurements were taken and averaged to determine the effective hydrodynamic diameter (Figure 1a). The results show that ball milling significantly reduces the average particle size. Particle size distributions for the original, filtered-only, and ball-milled plus filtered dispersions are shown in Figure 1b–d. Histograms were generated using ZetaPlus Particle Sizing Software (Brookhaven Instruments Corp., Upton, NY, USA, Version 5.23), and log-scaled x-axis labels were applied for better visualization. The original dispersion showed a narrow range dominated by large aggregates, with limited particle separation. In contrast, filtering and especially ball milling disrupted these agglomerates, producing a broader distribution of particle sizes.

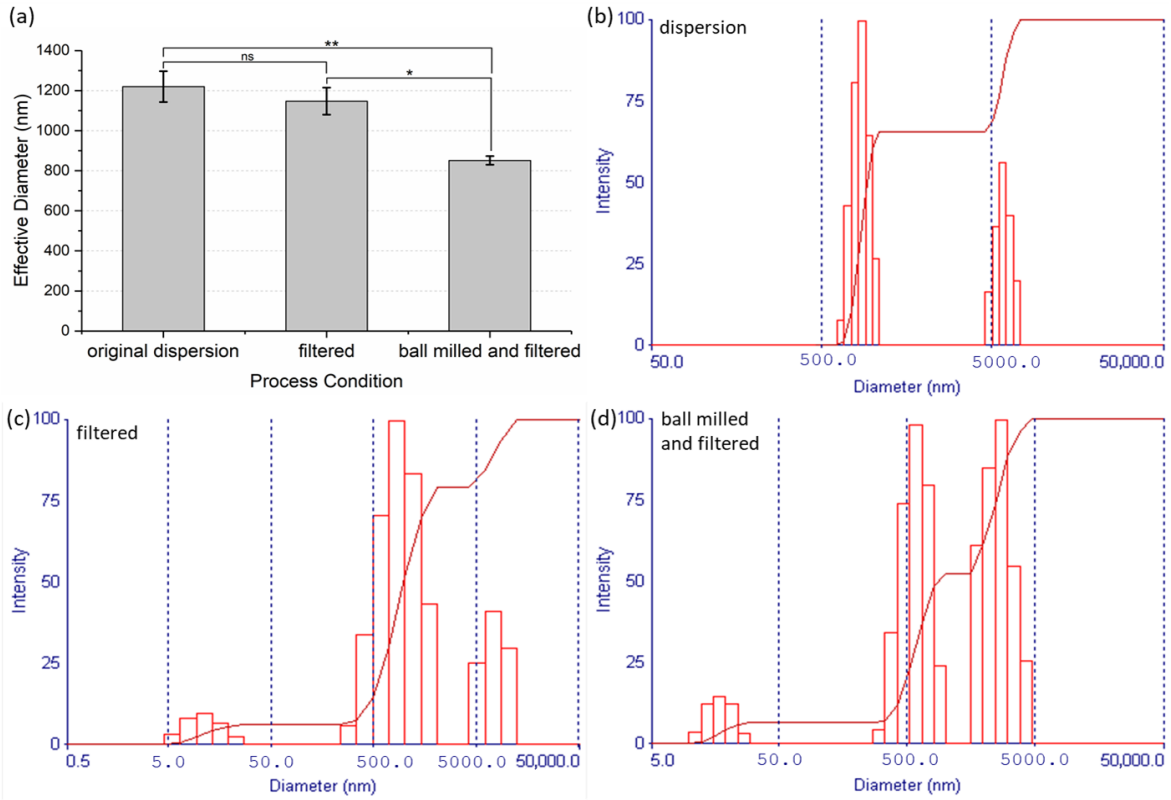


Figure 1. Dynamic light scattering (DLS) analysis of graphite dispersions processed under different conditions. (**a**) Effective hydrodynamic diameter of graphite particles across various processing methods. ns, not significant; * $p < 0.05$; ** $p < 0.01$. (**b**–**d**) Particle size distributions for (**b**) the original dispersion, (**c**) dispersion after filtration only, and (**d**) dispersion after ball milling followed by filtration. Ball milling reduces the average particle size and increases distribution breadth, indicating enhanced fragmentation and heterogeneity.

To evaluate differences in particle size across the three groups, a one-way analysis of variance (ANOVA) was performed on the hydrodynamic diameter data. The analysis yielded a p-value of 0.0023, indicating a statistically significant difference among the groups ($p < 0.05$). Post hoc Tukey's HSD testing revealed no significant difference between the original and filtered dispersions ($p = 0.6694$). In contrast, both the comparison between the original and ball-milled/filtered group ($p = 0.0026$, $p < 0.01$) and between the filtered and ball-milled/filtered group ($p = 0.0119$, $p < 0.05$) showed significant differences. These findings confirm that the observed reduction in particle size is due to the ball milling process rather than filtration alone.

SS substrates were coated either with graphite alone or with a polydopamine (PDA) interlayer followed by graphite, using the same method as in [20]. For PDA/graphite samples, a thin PDA film was first deposited via in situ oxidative polymerization: samples were immersed in an alkaline dopamine solution for 45 min, then rinsed and dried. The dried substrates were subsequently dipped into an aqueous graphite dispersion and withdrawn at a rate of 10 mm/min, followed by oven drying to remove residual moisture. Graphite-only samples were dip-coated directly onto bare steel without PDA treatment.

The PDA layer thickness was not measured in this study but has previously been characterized by our group using Atomic Force Microscopy (AFM) under identical deposition conditions, yielding values of approximately 50–120 nm [22,32,33]. Comparable thicknesses have also been reported by other groups for similar deposition durations [34,35]. Although PDA thickness was not optimized in this work, the deposition protocol used

reflects standard practice in our laboratory and provides a reliable baseline for comparison. All samples were cooled and stored under ambient conditions prior to testing.

As previously reported [20], the resulting graphite coatings exhibited an average surface roughness (Sa) of ~1 µm and an average thickness of ~6.4 µm, measured by laser scanning confocal microscopy (LSCM, VK-260, Keyence Corporation, Itasca, IL, USA).

Scanning electron microscopy (SEM) images (Figure 2) confirm that both graphite and PDA/graphite coatings exhibit similar surface morphologies. At low magnification (Figure 2a,d), both coatings appear uniform in coverage. At intermediate magnification (Figure 2b,e), small surface asperities become visible. At higher magnification (Figure 2c,f), the porous structure of individual graphite flakes is clearly observed. The presence of the PDA underlayer does not significantly alter the surface topography or flake distribution of the graphite coating. However, the PDA/graphite surface exhibits a slightly denser and smoother appearance in the imaged region compared to the graphite-only coating.

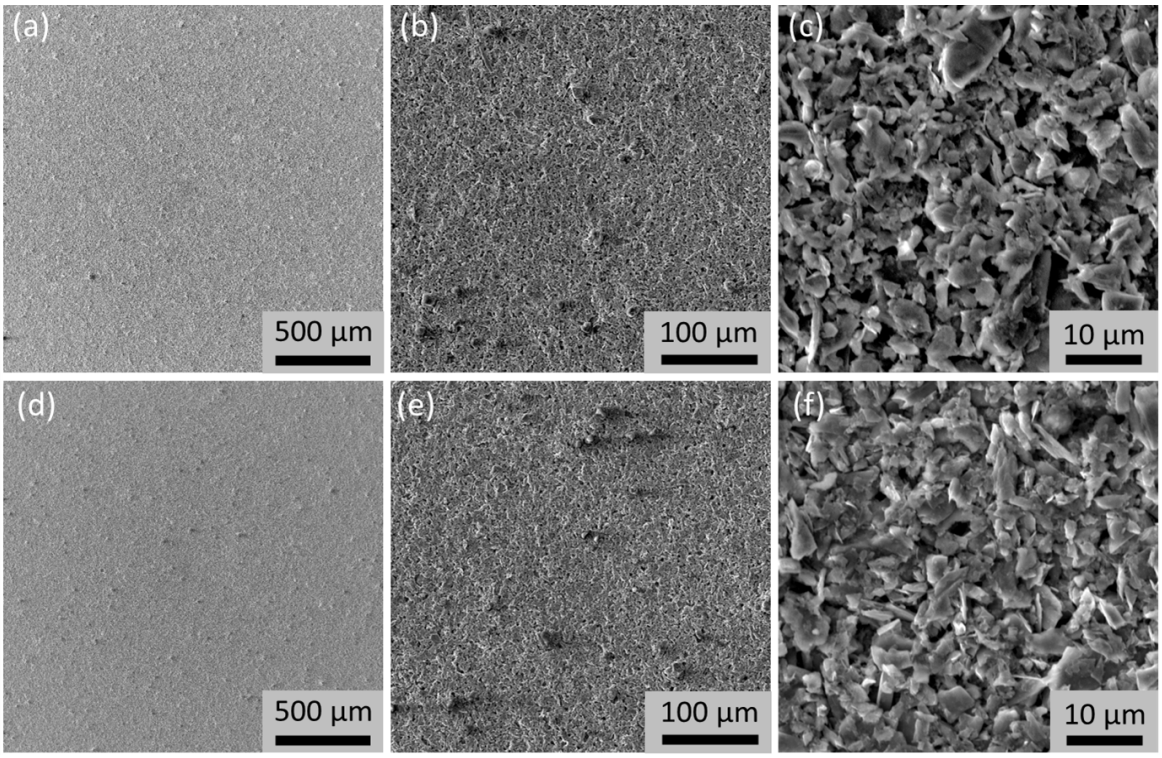


Figure 2. SEM images of graphite and PDA/graphite coatings prior to wear testing, captured at multiple magnifications to compare surface morphology. (**a**–**c**) Graphite-only coating; (**d**–**f**) PDA/graphite coating. Images correspond to increasing magnification levels: (**a**,**d**) 2 mm × 2 mm, (**b**,**e**) 400 µm × 400 µm, and (**c**,**f**) 50 µm × 50 µm.

2.3. Tribological Testing

The tribological performances of the graphite and PDA-modified graphite coatings was evaluated using a reciprocating ball-on-flat configuration on a Universal Mechanical Tester (UMT-3, Bruker Inc., Billerica, MA, USA). A 6.35 mm stainless steel ball was used as the counterface, consistent with the setup employed in our prior scratch adhesion study [20]. All tests were conducted under dry sliding conditions at room temperature, using linear reciprocation with a 5 mm stroke length, a 5 N normal load (corresponding to an estimated Hertzian contact pressure of ~1.12 GPa, excluding coating effect), and a sliding speed of 1 mm/s (0.1 Hz). Data was recorded every 0.1 seconds and the tribometer was set to stop the test when the friction force exceeded the COF threshold for four consecutive measurements.

Three testing protocols were employed to capture both short-term and long-term performance:

1. 2-cycle tests (~20 s duration) to characterize initial sliding behavior and early-stage wear.
2. 1 h tests to assess steady-state friction and wear resistance under prolonged cycling.
3. Run-to-failure tests, where sliding continued until the COF exceeded 0.5, indicating coating failure. The time to failure was recorded as the coating lifetime.

These protocols enabled a systematic comparison of friction behavior, wear progression, and transfer film formation across multiple timescales. The durations were chosen to isolate the interfacial shear response before transfer film formation (2-cycle tests), to capture the effect of transfer film development and compaction on stabilized friction behavior (1 h tests), and to reflect complete coating removal and exposure of the steel substrate as a standard measure of solid lubricant failure (run-to-failure tests). For each test condition, three replicates were conducted per coating type. Error bars presented in figures represent the standard deviation across replicates.

2.4. Characterization

2.4.1. Morphology and Surface Topography

Surface morphology and topography were analyzed using an SEM (VEGA3, TESCAN ORSAY HOLDING, Brno, Czech Republic) and an LSCM. The SEM was operated at 10 kV accelerating voltage with a 16 mm working distance, enabling high-resolution imaging of the wear tracks. The LSCM was used to evaluate surface topography of both pristine and worn coatings, as well as to characterize transfer films and wear scars on the steel ball counterface. While the morphology of the pristine coatings is briefly shown in Figure 2, this study primarily focuses on surface changes after reciprocating wear tests.

2.4.2. Elemental Analysis

Energy-dispersive X-ray spectroscopy (EDS) was performed using an SEM equipped with an EDS detector (Nova 200 NanoLab, FEI, Hillsboro, OR, USA) to assess elemental composition within and around the wear tracks. Elemental mapping and line scans of carbon (C), iron (Fe), and chromium (Cr) were used to evaluate graphite coating retention and identify regions of substrate exposure. EDS analysis was conducted on worn surfaces of both graphite-only and PDA/graphite-coated samples.

2.4.3. Raman Analysis

Raman spectroscopy was performed using a Horiba Jobin Yvon LabRAM HR spectrometer (Palaiseau, France) equipped with a silicon charge-coupled device (CCD) camera detector (Andor iDus 420A-OE-325, Belfast, UK). A 632.8 nm He–Ne laser (Melles Griot, 05-LPL-915-070, Carlsbad, CA, USA) served as the excitation source due to its suitability for characterizing carbonaceous and organic materials. The laser was focused to a ~2 μm diameter spot using a 100× objective lens (numerical aperture, NA = 0.9), and the spectral resolution was determined by a 1.2 mm confocal aperture and 1800 lines/mm diffraction grating. Laser power was kept below 1 mW to prevent thermal damage to the soft coatings.

Spectra were acquired from five key regions: (1) bare stainless steel (control), (2) PDA-coated stainless steel, (3) pristine graphite coating, (4) wear debris within the wear track, and (5) worn surface within the wear track. These locations were selected to capture tribo-induced structural evolution and baseline material signatures. Both graphite-only and PDA/graphite coatings were evaluated after 1 h of sliding to enable direct comparisons under equivalent test conditions.

For each coating group, three independent samples were analyzed. On each sample, spectra were collected at one pristine coating location, three wear-debris sites, and

three worn regions, totaling seven spectra per sample and 21 spectra per coating group. Additional spectra were obtained from multiple points on the stainless steel and PDA-only surfaces to characterize substrate and underlayer features. Each spectrum was collected with a 5 s integration time and two accumulations per scan at room temperature. Sample points were randomly selected to account for surface heterogeneity.

Raw Raman spectra were processed using OriginLab 2017 (OriginLab Corp., Northampton, MA, USA). Baseline correction was applied using adjacent-averaging based on the second derivative of the selected spectrum. All spectra were normalized to a 0–1 intensity scale for comparison. The D-band (~1330–1360 cm^{-1}) and G-band (~1580–1600 cm^{-1}) were identified for all spectra, consistent with graphitic carbon literature [36,37]. The intensity ratio (I_D/I_G) was calculated using peak height and served as an indicator of structural disorder [38,39]. Error bars presented in subsequent figures represent the standard deviation of replicate measurements across samples and regions.

2.4.4. X-Ray Photoelectron Spectroscopy (XPS) Analysis

XPS was performed using a PHI 5000 VersaProbe (ULVAC-PHI, Kanagawa, Japan) to determine the elemental composition and chemical bonding at the wear track surfaces. Given the surface sensitivity of the technique (sampling depth ~10 nm), scans were limited to regions where the coating had worn sufficiently to allow interface-level investigation. Therefore, XPS analysis was conducted on both SS/graphite and SS/PDA/graphite samples following two conditions: (1) 1 h sliding tests, and (2) extended tests continued until coating failure (defined by COF $\geq$ 0.5). Each survey spectrum was collected for at least 45 min.

3. Results and Discussion

3.1. Friction

Figure 3 presents the COF and wear life of graphite and PDA/graphite coatings under various test conditions. The shades of the same color indicate multiple runs of the tests on various samples of graphite (black-grey) and PDA/graphite (red-orange). In the short-duration 2-cycle tests (Figure 3a), both coatings show an initial rapid increase in COF to 0.25–0.3. The sharp periodic drops every 5 s correspond to deceleration at the end of each stroke. Notably, the graphite coating displays more pronounced COF fluctuations within each cycle, attributed to its inherently easy-sliding nature, which leads to intermittent and inconsistent contact with the counterface. In contrast, the PDA/graphite coating exhibits slightly higher but more stable COF values, consistent with prior findings [20]. A subtle downward trend in COF is observed toward the end of the 20 s test for PDA/graphite.

This decreasing COF trend becomes more evident during the 1 h tests (Figure 3b). The shaded regions representing standard deviation show greater variability in COF for PDA/graphite throughout the test. Both coatings experience a COF reduction from ~0.25 to 0.1–0.15 within the first 10 min. The graphite coating reaches a steady-state COF of ~0.1 in under 5 min, whereas the PDA/graphite coating takes nearly twice as long to reach ~0.125. The higher COF of PDA/graphite compared to graphite alone can be explained by two key factors. First, PDA enhances interfacial adhesion; which restricts the mobility and realignment of graphite flakes; a known mechanism for friction reduction in graphite [30]. Second, PDA itself exhibits relatively high adhesive and frictional forces on various surfaces [39,40]. Consequently, it is often used sparingly in composite coatings to balance adhesion and friction [41]. During sliding, intermixing at the PDA–graphite interface likely contributes to the higher and more variable COF observed. Nonetheless, both the average COF and its variability decrease over time for PDA/graphite, reflecting a gradual transition to stable sliding.

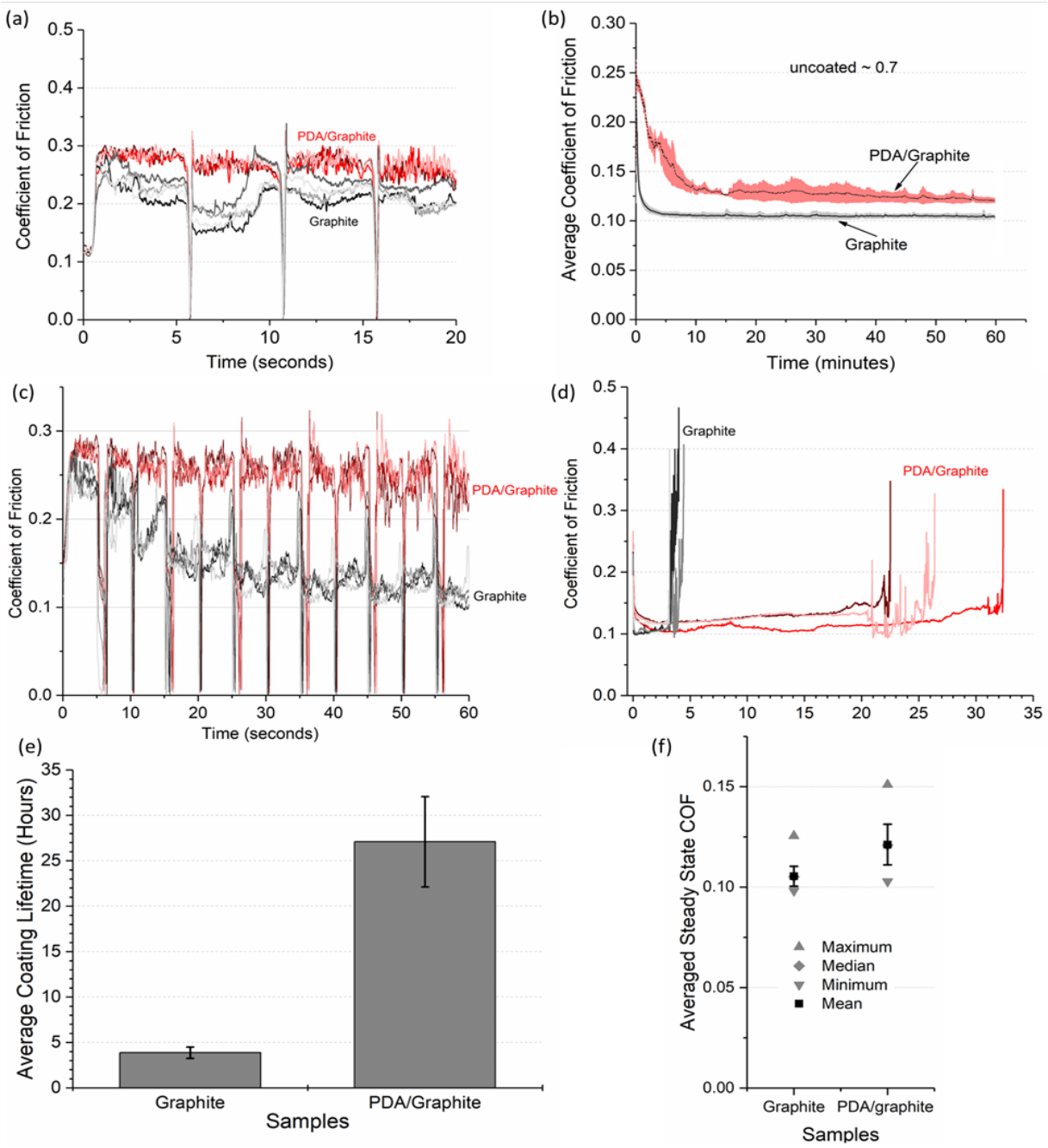


Figure 3. Friction behavior and wear life of graphite and PDA/graphite coatings under dry sliding. (**a**) COF profiles during short 2-cycle sliding tests. (**b**) Average COF over time during 1 h tests; shaded areas represent standard deviations. (**c**) Enlarged view of the first minute of the 1 h tests, emphasizing run-in behavior during the initial six cycles. (**d**) COF evolution during extended sliding tests conducted until coating failure. (**e**) Average lifetime of each coating based on failure test duration. (**f**) Steady-state COF distributions from failure tests, showing mean, median, standard deviation, and range (minimum to maximum). Color shades indicate replicates within the same group and across samples.

Ultimately, both coatings achieve low steady-state COFs: ~0.105 for graphite and ~0.12 for PDA/graphite, values significantly lower than that of unlubricated steel (~0.7). These results confirm that both systems effectively reduce friction, albeit through distinct mechanisms.

To better visualize early frictional behavior, the first minute of the 1 h test (i.e., initial six cycles) is shown in Figure 3c. These initial cycles closely mirror the 2-cycle test results,

with COF ranging between 0.25 and 0.3. However, Figure 3c more clearly illustrates the differing run-in behaviors of the coatings. Graphite undergoes a rapid decline in COF, indicating a short run-in period, while PDA/graphite exhibits a more gradual reduction, reflecting an extended run-in phase.

Figure 3d presents COF evolution during run-to-failure tests. Initially, graphite shows lower COF than PDA/graphite, but fails abruptly after several hours, as indicated by a sharp COF rise. In contrast, PDA/graphite maintains a relatively stable COF over a significantly longer period, with a more gradual increase preceding failure. As shown in Figure 3e, PDA/graphite coatings endured an average of 9755 cycles (~27 h) before failure, compared to 1397 cycles (~3.8 h) for graphite, a sevenfold improvement. This difference of 8358 cycles is statistically significant (One-way ANOVA and *t*-test, $p = 0.0013$). Prior scratch testing demonstrated PDA's role in enhancing graphite adhesion under increasing loads [20]; here, the data show that this benefit extends to long-term sliding, with PDA substantially improving wear resistance and coating integrity.

Finally, Figure 3f compares steady-state COFs measured during long-duration tests: 4 h for graphite and 20 h for PDA/graphite. Graphite coatings show narrower COF distributions, likely due to efficient flake transfer and redistribution within the wear track. In contrast, PDA/graphite coatings exhibit broader COF variability, yet maintain surface coverage for far longer, highlighting their superior durability despite greater friction variability.

Overall, Figure 3 demonstrates that while PDA increases friction modestly, it enables more stable sliding and significantly extends coating life, increasing wear resistance by a factor of seven. The interplay between friction and wear mechanisms is explored in more detail in Figures 4–7.

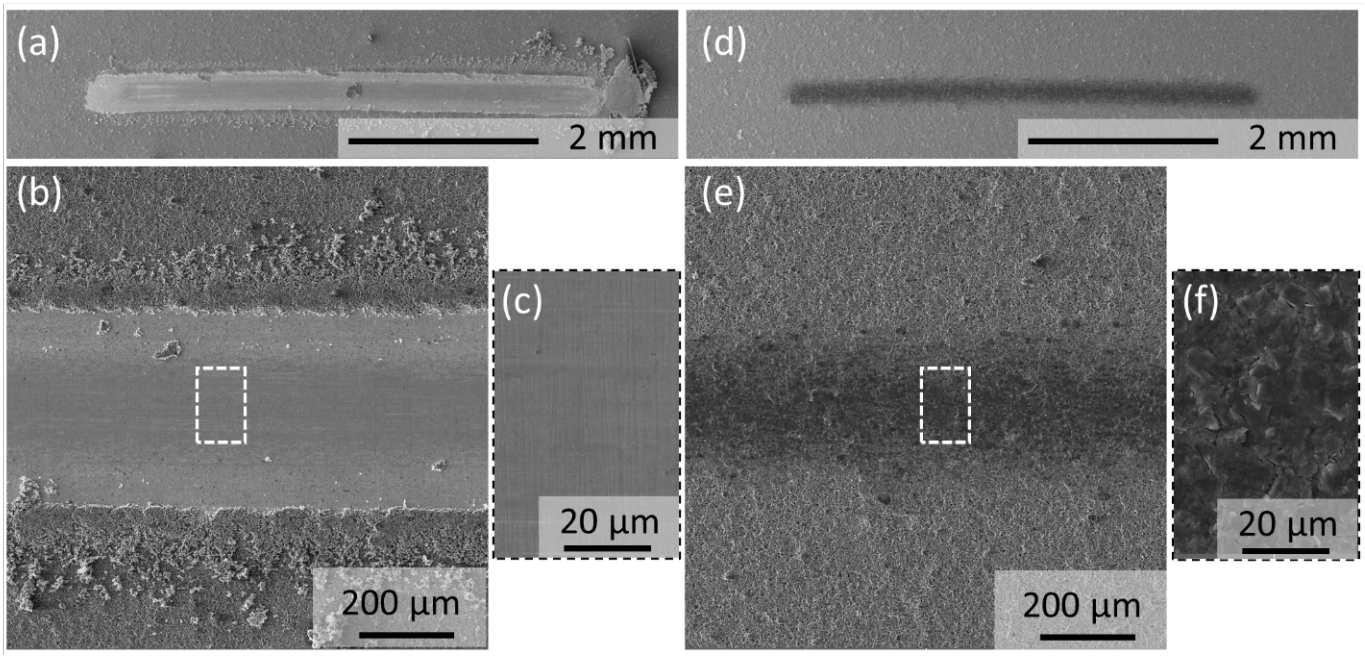


Figure 4. SEM analysis of wear tracks after two sliding cycles. (**a**–**c**) Graphite coatings and (**d**–**f**) PDA/graphite coatings. (**a**,**d**) Full-track overviews; (**b**,**e**) 1 mm × 1 mm regions near the track center; (**c**,**f**) high-magnification images of boxed areas in (**b**) and (**e**), respectively.

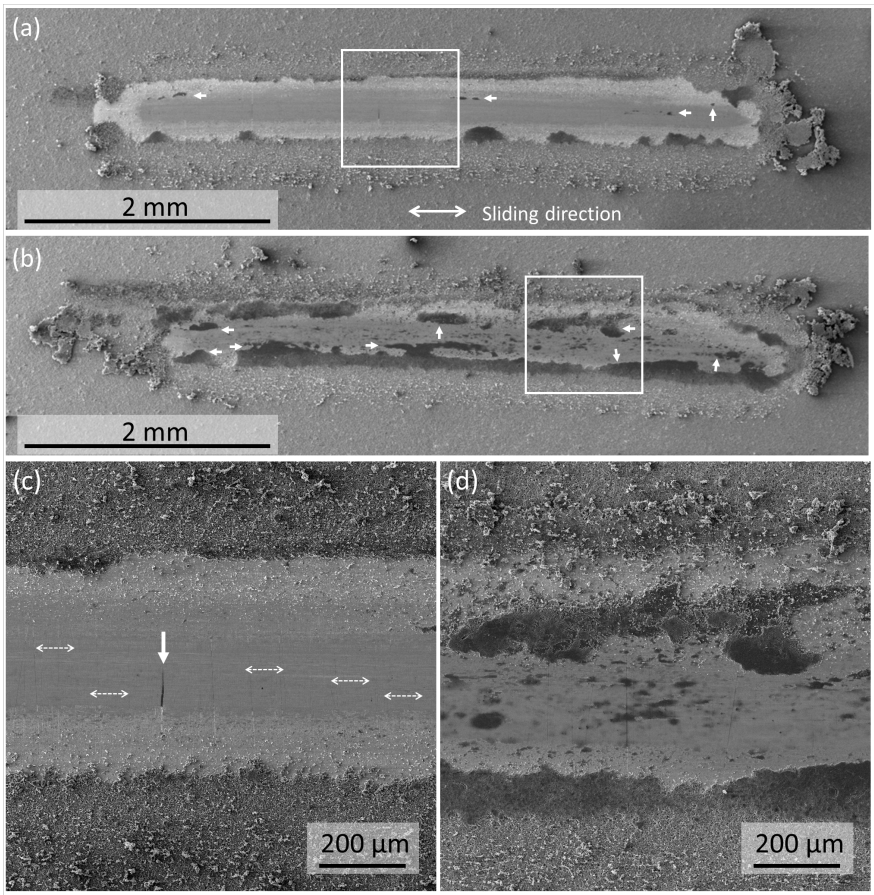


Figure 5. SEM images of wear tracks after 1 h sliding. (**a**,**b**) Full-track overviews for graphite and PDA/graphite coatings, respectively. Arrows indicate regions of compacted graphite remaining within the wear path. (**c**,**d**) Higher-magnification views corresponding to boxed regions in (**a**,**b**). In (**c**), the solid arrow highlights a groove filled with compacted graphite, while the dotted arrows indicate abrasion grooves aligned with the sliding direction.

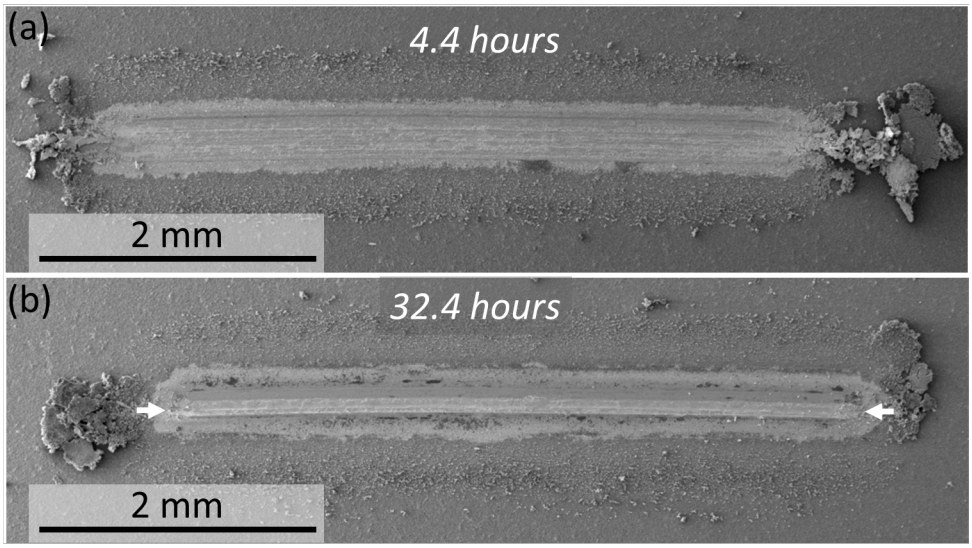


Figure 6. Representative SEM images of wear tracks after coating failure. (**a**) Graphite and (**b**) PDA/graphite coatings following run-to-failure sliding tests, highlighting differences in material retention and surface degradation. Arrows in (**b**) mark localized regions of severe wear along the sliding direction.

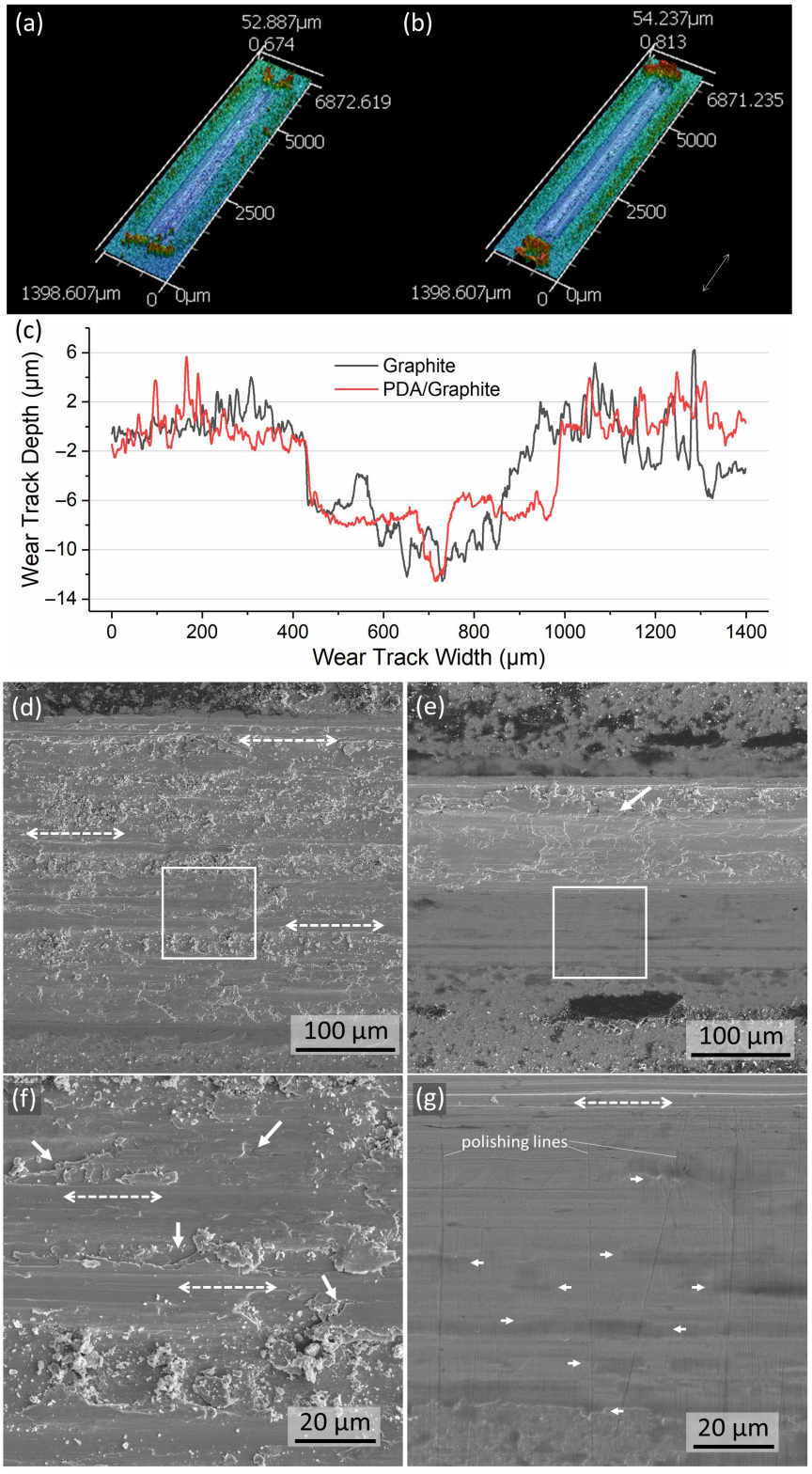


Figure 7. Topographical and high-resolution SEM characterization of wear tracks following coating failure. (**a**,**b**) 3D surface maps of the wear regions. (**c**) Height profile comparison across wear tracks. (**d**,**e**) SEM images of the central wear track at 400 µm × 400 µm. (**f**,**g**) Higher-magnification SEM images (100 µm × 100 µm) of boxed areas in (**d**,**e**). Graphite coatings are shown in the left column; PDA/graphite coatings are in the right. Single arrows in (**e**,**f**) denote regions of adhesive wear. Double-headed arrows in (**d**,**f**,**g**) indicate abrasion marks and grooves. Arrows in (**f**) highlight scuff marks, torn regions, and deep furrows of the exposed substrate. Arrows in (**g**) highlight compressed PDA/graphite coating where original polishing lines remain visible.

3.2. Wear Track Morphology and Mechanisms

SEM imaging after 2-cycle wear tests reveals striking differences in wear track morphology. The slight curvature seen in Figure 4a,d arises from the widefield lens used to capture the full track. In Figure 4a, graphite coating material is visibly displaced to the right side of the wear path, leaving much of the track nearly bare. This lateral displacement beyond the ball contact area aligns with graphite's known low adhesion behavior [18,20] and suggests a plowing-dominated wear mechanism. In contrast, the PDA/graphite coating in Figure 4d remains largely intact, with only a slightly darkened track marking the ball's sliding path.

High-magnification images provide additional insight. The graphite wear track (Figure 4b,c) appears mostly barren, with only a few residual particles scattered along the wear path. In contrast, the PDA/graphite wear track (Figure 4e,f) displays compressed graphite flakes without significant material removal. This compaction behavior is consistent with previous single-pass scratch tests performed under increasing normal loads [20]. Denser graphite films exhibit greater resistance to wear, and PDA-enhanced adhesion facilitates this compaction mechanism, preventing premature coating loss.

Figure 5 shows SEM images of wear tracks after 1 h sliding tests. In both coatings, some substrate exposure and material pile-up are evident at the edges of the track. However, the graphite-coated sample shows a largely cleared wear path, with only isolated islands of compressed graphite remaining (see arrows in Figure 5a). In contrast, the PDA/graphite sample retains significantly more compacted material within and around the wear track (see arrows in Figure 5b), indicating improved coating retention and resistance to detachment during prolonged sliding.

High-magnification SEM images (Figure 5c,d) further illustrate contrasting wear modes. The graphite-coated surface exhibits extensive material loss, with only a narrow strip of compacted graphite remaining (solid arrow, Figure 5c). Additionally, shallow grooves aligned with the sliding direction (dotted arrows, Figure 5c) suggest abrasive wear caused by hard counterface asperities. These features likely darkened the region where direct contact occurred. By contrast, the PDA/graphite sample retains broader graphite coverage across the wear zone. Evidence of material transfer and compaction is observed within the track, implying that PDA improves interfacial bonding among graphite flakes, reducing coating loss and supporting in situ realignment and densification during sliding.

Figure 6 presents SEM images of wear tracks at the point of coating failure, defined as the time when COF rose to 0.5, approaching the steel-on-steel friction baseline. Prolonged sliding under dry conditions led to increased wear due to elevated contact stress, expanded real contact area, and frictional heating effects [42]. As shown in Figure 6a, the graphite-coated sample exhibits substantial material pile-up and a rough, irregular surface, in contrast with the relatively smooth track after 1 h (Figure 5a). The polishing marks, still visible in earlier tests and oriented perpendicular to sliding, have vanished, indicating a shift from mild plowing to more severe abrasive and adhesive wear mechanisms.

The PDA/graphite sample in Figure 6b also shows signs of wear but endured 28 additional hours of sliding compared to graphite alone before reaching the COF failure threshold. Wear appears localized to a smaller central region (see arrows), suggesting that final failure occurred under localized high stress. The enhanced adhesion from PDA helped retain graphite in the wear zone and inhibited lateral wear propagation, delaying catastrophic failure. Additional surface morphological features are examined in Figure 7.

The 3D surface maps (Figure 7a,b) illustrate the topography of the wear tracks, revealing clear morphological differences between the coatings. Cross-sectional profiles (Figure 7c) show that the graphite sample exhibits deeper grooves, indicative of severe wear, while the PDA/graphite sample displays a much shallower profile, limited to the

original coating thickness—even after a test duration roughly seven times longer. Wear in the PDA/graphite sample is localized to a narrow central region, contrasting with the more widespread degradation seen in the graphite sample. This localization likely results from higher contact pressure and lubricant depletion, with PDA improving adhesion and thereby restricting steel-on-steel contact to a smaller area.

SEM images (Figure 7d–g) further illustrate the dominant wear mechanisms. In the graphite sample (Figure 7d), roughened surfaces and fine debris suggest a combination of abrasive and adhesive wear. Abrasive wear is evident from parallel scratch marks along the sliding direction (double-headed arrows in Figure 7d). Adhesive wear is seen as scuff marks, torn regions, and deep furrows (arrows in Figure 7f), commonly associated with temporary micro-welding and shear at the interface between the sliding steel counterface and exposed substrate. This is typical of steel-on-steel contact under high load in the absence of a protective layer.

In contrast, the PDA/graphite sample (Figure 7e) retains visible polishing marks, indicating that most of the surface coating remains intact. Only a small region exhibits adhesive wear (arrow in Figure 7e). Significant graphite coverage remains, highlighting the role of PDA in enhancing graphite retention. Higher-magnification images (Figure 7f,g) confirm this contrast: the graphite sample displays severe abrasion and material loss (arrows in Figure 7f, while the PDA/graphite surface retains compressed and well-adhered graphite (arrows in Figure 7g), suggesting improved interfacial bonding and reduced material detachment. Together, these observations underscore the enhanced durability of graphite coatings modified with a PDA underlayer.

3.3. Elemental Analysis of Wear Tracks

To assess material retention and confirm the composition of worn regions, EDS was conducted on both coatings after 1 h sliding and at the point of failure. The primary elements analyzed were carbon (C), originating from the graphite coating and PDA underlayer, and iron (Fe) and chromium (Cr), from the SS substrate. Although SS contains a small amount of carbon (typically 0.03–0.15%), its contribution to the total carbon signal is negligible compared to the ~6.4 µm-thick graphite layer. Similarly, the PDA interlayer, being only ~50–100 nm thick, contributes minimally to the EDS signal, which typically penetrates ~1 µm into the surface.

Full elemental scans of the wear tracks revealed additional signals, with oxygen being prevalent across the scanned area. Oxygen intensity was especially concentrated over regions of exposed substrate, consistent with the formation of iron oxides (Fe_2O_3 and Fe_3O_4) on the steel surface. Other detected elements included Ni (from steel), Si and Na (likely residual dispersants from the graphite suspension), and N and O contributions from environmental exposure. For relevance to coating retention and wear mechanisms, the analysis in the main text focuses on C, Fe, and Cr to distinguish coating coverage from substrate exposure. Full elemental scans are provided in the Supplementary Information (Figures S1 and S2).

Figure 8 presents SEM and EDS results following 1 h sliding tests. SEM micrographs and the regions selected for EDS mapping and line scans are shown in Figure 8a,d. In the graphite-coated sample (Figure 8a–c), strong Fe and Cr signals indicate that the coating was either removed or thinned below the detection limit. In contrast, the PDA/graphite sample (Figure 8d–f) retains prominent carbon signals within parts of the wear track (arrow in Figure 8f), confirming that graphite remains present in the contact zone. Elemental mapping (Figure 8e) further reveals carbon-rich patches inside the wear scar, consistent with a compaction-dominated wear mechanism and enhanced retention in the PDA/graphite system. These results support the proposed mechanism: graphite coatings primarily fail

through plowing and material removal, while PDA/graphite coatings undergo localized compression and benefit from stronger interfacial adhesion that reduces material loss [20].

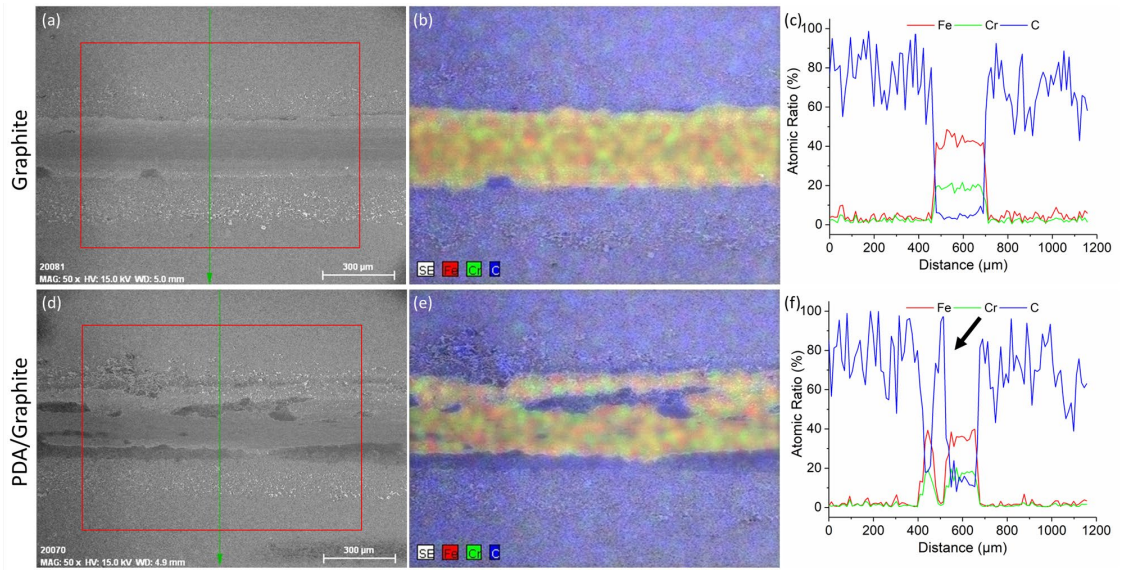


Figure 8. SEM and EDS analysis of wear tracks after 1 h sliding tests. (**a**,**d**) SEM images of wear regions (red rectangle: elemental map region; green arrow: line scan). (**b**,**e**) Elemental maps of C, Fe, and Cr. (**c**,**f**) EDS line scans across the wear tracks for graphite and PDA/graphite coatings, respectively. Arrow in (**f**) indicates retained graphite in the PDA/graphite sample wear track.

Figure 9 shows SEM and EDS mapping after the coatings reached failure, defined by a COF of 0.5. The top row (Figure 9a–d) corresponds to graphite, and the bottom row (Figure 9e–h) to PDA/graphite. In both cases, Fe and Cr are clearly present in the wear tracks, indicating exposure of the substrate. However, carbon mapping reveals a critical difference: in the graphite sample (Figure 9d), the wear track shows no carbon signal, confirming complete coating removal. Conversely, the PDA/graphite sample (Figure 9h) retains carbon-rich areas even after extended sliding and high contact stress (>1 GPa), as marked by arrows. This residual carbon indicates that parts of the graphite coating remained intact, further highlighting PDA's role in improving graphite retention, enhancing wear resistance, and protecting the substrate under severe tribological conditions.

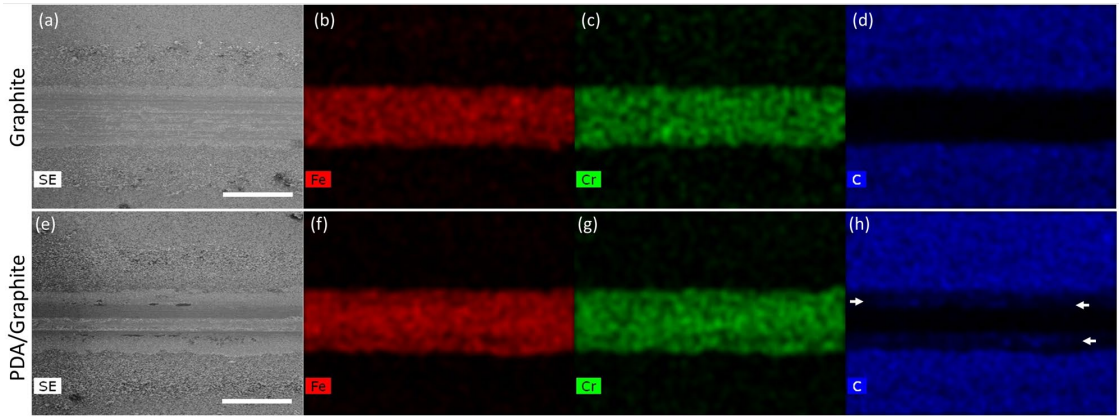


Figure 9. EDS mapping of wear tracks after failure. (**a**,**e**) SEM micrographs of selected wear regions; (**b**,**f**) Iron (Fe); (**c**,**g**) Chromium (Cr); and (**d**,**h**) Carbon (C) maps for graphite and PDA/graphite coatings, respectively. Arrows in (**h**) highlight retained graphite in the PDA/graphite wear track. Scalebar = 300 μm.

3.4. Transfer Film and Counterface Wear

Figure 10 presents optical and 3D surface characterizations of the steel counterface balls after sliding tests to evaluate transfer film formation and wear behavior for both graphite and PDA/graphite coatings at three test stages: after 2 cycles (20 s), 1 h, and until failure. Figure 10a–f show 10× optical images, while Figure 10(a1–f1) and (a2–f2) provide higher-magnification optical and 3D profilometry views, respectively.

At the earliest stage (Figure 10a,d), graphite (Figure 10a) shows substantial material transfer to the ball surface, forming a loose, irregular deposit. In contrast, the PDA/graphite counterpart (Figure 10d) remains clean with no visible transfer. This early contrast suggests that PDA initially inhibits graphite detachment and suppresses premature transfer film formation.

After 1 h of sliding (Figure 10b,e), both coatings produce more coherent transfer films. The graphite coating's counterface ball (Figure 10b) shows an elliptical wear scar with a uniform transfer layer. The PDA/graphite coating's counterface ball (Figure 10e) displays a smoother film at the center, surrounded by darker, patchier zones of adhered debris. These differences are clearer in Figure 10(b1,e1): graphite exhibits continuous film coverage, while PDA/graphite reveals localized debris clusters. The corresponding ball wear scar for PDA/graphite is smaller than that observed with the graphite-only coating. The 3D maps (Figure 10(b2,e2)) confirm that graphite forms a thin, uniform layer, whereas PDA/graphite produces irregular surface buildup, likely due to the increased adhesiveness from PDA and retention of compacted particles.

Upon sliding to failure (Figure 10c,f), the divergence in wear behavior becomes more pronounced. The graphite-coated ball (Figure 10c) exhibits severe abrasion, deep grooves, and loss of transfer film—corroborating the substrate exposure seen earlier (e.g., Figure 5c). In contrast, the PDA/graphite ball (Figure 10f) maintains a relatively thick, cohesive transfer film with a confined wear zone. The localized film retention is evident in Figure 10(f1), and the corresponding 3D map (Figure 10(f2)) highlights a raised film with only limited surface damage.

Overall, graphite coatings evolve from loose, early-stage transfer (Figure 10a–a2), to smooth conformal films (Figure 10b–b2), and eventually to degraded, heavily worn surfaces (Figure 10c–c2). In contrast, PDA/graphite coatings begin with minimal transfer (Figure 10d–d2), develop patchy but adherent films over time (Figure 10e–e2), and ultimately form robust, protective layers with localized wear (Figure 10f–f2). These results underscore the critical role of stable, cohesive transfer films in minimizing friction and protecting surface asperities during sliding [43].

The PDA interlayer appears to enhance interfacial adhesion and transfer film cohesion, delaying detachment and promoting buildup. Compared to the graphite system, where particle coverage decreases with time, the PDA/graphite counterpart exhibits substantial late-stage film accumulation—supporting a mechanism of PDA-mediated flake anchoring and material retention.

Previous studies suggest that tribofilm formation is often aided by chemical reactions, such as metal oxide generation on steel surfaces [44], passivation of dangling bonds in graphite [42,45], or the formation of turbostratic carbon structures via graphite rearrangement and hybridization shifts during sliding [45]. In this system, PDA likely alters those dynamics by improving chemical bonding and surface adhesion. Further analysis of bonding behavior and hybridization states is provided in Section 3.5 using Raman spectroscopy (Figure 11).

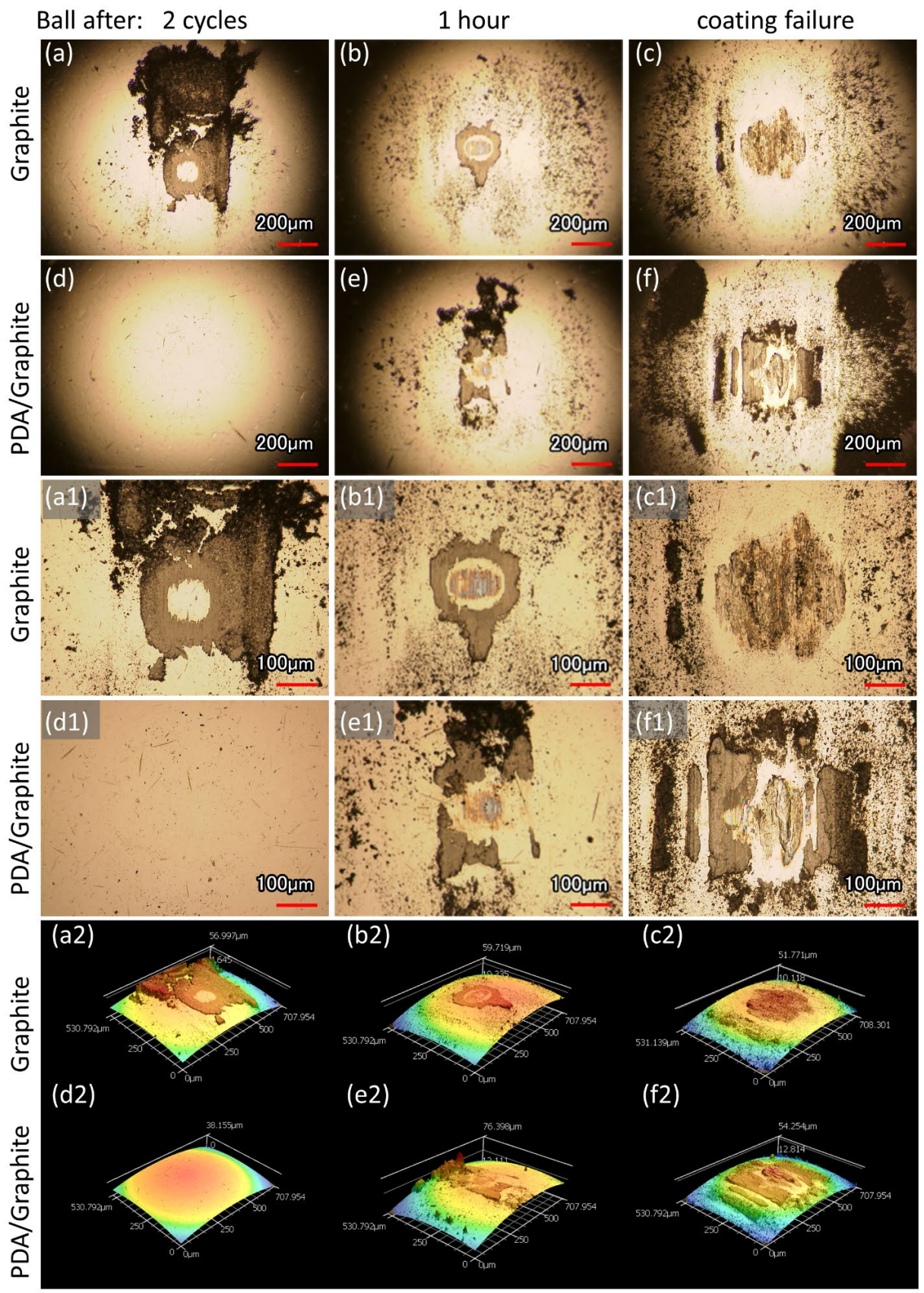


Figure 10. Optical and 3D profilometry images of counterface balls after sliding tests. (**a**–**c**) Graphite and (**d**–**f**) PDA/graphite coatings after: (**a**,**d**) 2 cycles (20 s); (**b**,**e**) 1 h sliding; and (**c**,**f**) sliding until failure. (**a1**–**f1**) Higher-magnification optical views of wear scars. (**a2**–**f2**) 3D surface maps corresponding to (**a1**–**f1**).

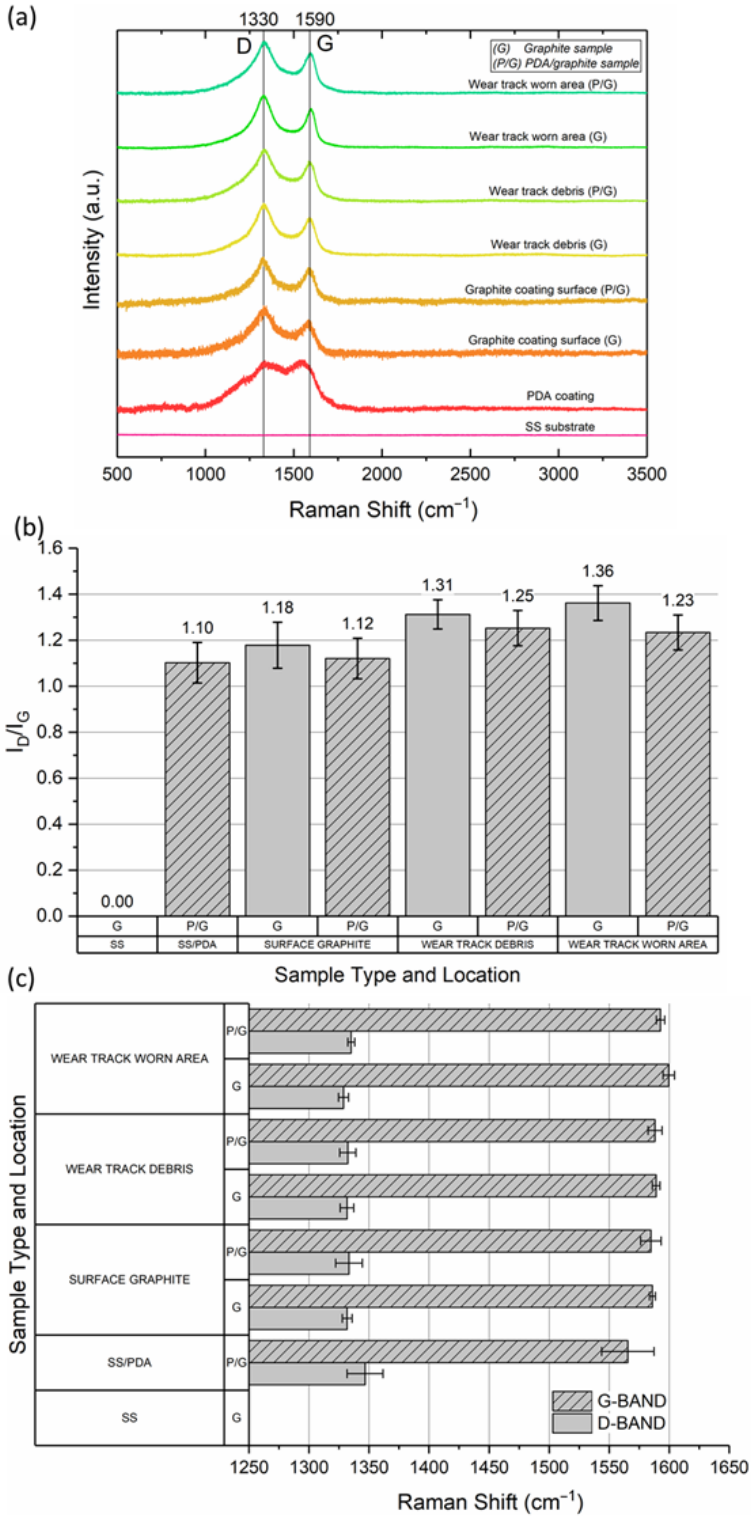


Figure 11. Raman spectroscopy of graphite and PDA/graphite coatings. (**a**) Spectra from various surface and wear track regions after 1 h tests. (**b**) Averaged I_D/I_G ratios for each location (**c**) Averaged Raman shift in D and G bands of various regions. Error bars indicate standard deviation.

3.5. Raman Spectra Analysis

Raman spectroscopy was used to evaluate bonding structure, structural disorder, and sliding-induced changes in graphite and PDA/graphite coatings. This technique is ideal for carbon-based materials due to its sensitivity to sp^2/sp^3 hybridization and short-range ordering. The G-band (~1580–1600 cm^{-1}) arises from in-plane vibrations of sp^2-hybridized

carbon atoms and reflects graphitic crystallinity, while the D-band (~1330–1360 cm^{-1}) corresponds to disordered or defected structures and sp^3 content [36,37].

Figure 11a presents representative spectra collected from eight surface areas: stainless steel (SS), PDA-coated steel (SS/PDA), surface of graphite (G) and PDA/graphite (P/G) coatings, wear debris and worn regions within the wear tracks from each coating. All carbon-containing regions exhibited prominent D and G bands, while SS displayed no significant Raman features in this range.

Figure 11b quantifies the intensity ratio (I_D/I_G), which reflects structural disorder. The SS sample yielded $I_D/I_G = 0.00$, as expected. The PDA layer exhibited broad peaks centered at ~1345 and 1565 cm^{-1}, with an average I_D/I_G of 1.10 ± 0.09. This value falls within the reported range of ~0.7–1.6 for PDA in prior studies and is consistent with amorphous carbon structures comprising C–C bonded indole-like units [25,39,46–50]. The presence of amide nitrogen and catechols—known to enhance D-band intensity—further supports this interpretation [51].

The surface regions of pristine graphite and PDA/graphite coatings showed sharper D and G bands with moderate disorder levels, yielding I_D/I_G values of 1.18 (G) and 1.12 (P/G), respectively. These values are higher than those of highly crystalline graphite ($I_D/I_G < 0.1$), reflecting the turbostratically stacked, flake-based coatings with edge-exposed microstructures seen in Figure 2.

Following 1 h sliding, wear debris and worn track regions exhibited modest increases in I_D/I_G. For wear debris, the ratios were 1.31 (G) and 1.25 (P/G); for worn regions, 1.36 (G) and 1.23 (P/G). While one-way ANOVA revealed group-level variance, Tukey's HSD post hoc analysis indicated that only a few comparisons were statistically significant. Overall, this suggests that tribological loading caused local increases in defect density but did not drastically alter bonding structure.

Figure 11c tracks shifts in D- and G-band positions across all sample types. The G-band showed a small shift toward higher wavenumbers in worn and debris regions, which is often attributed to compressive stress, decreased domain size, or tribo-induced strain. However, due to overlapping standard deviations, these shifts should be interpreted cautiously. D-band positions remained relatively stable.

Notably, this is the first Raman analysis (to our knowledge) specifically examining tribo-induced evolution in coatings with PDA underlayers, rather than PDA-blended or encapsulated systems. Taken together, the Raman results indicate that sliding-induced changes in both graphite and PDA/graphite coatings are modest, with only slight increases in I_D/I_G and minor G-band shifts observed in worn regions and debris. These findings suggest that the overall graphitic bonding structure is largely preserved under tribological stress. SEM observations of flake compaction and surface roughening (Figures 5, 7 and 8) further support the conclusion that the PDA/graphite interface enhances structural resilience under shear and frictional load, helping maintain coating integrity.

3.6. XPS Analysis

To investigate the surface chemistry and coating integrity following tribological testing, XPS survey spectra were collected from the wear tracks of SS/graphite and SS/PDA/graphite samples. Two conditions were examined: (i) after 1 h of sliding (COF < 0.5), and (ii) after continued sliding until coating failure (COF ≥ 0.5). XPS probes the outermost ~10 nm of the surface, enabling detection of chemical composition and substrate exposure in worn regions.

Figure 12 shows the XPS survey spectra acquired from representative wear regions. In the 1 h condition (Figure 12a,b), the spectra were dominated by C 1s peaks from the

graphite coating and Na KLL peaks, likely originating from dispersants used in the aqueous graphite formulation. Additional signals included O 1s, N 1s, F 1s, Si 2s, and Si 2p, which may arise from environmental adsorption, trace contaminants, or residual processing additives. Notably, Fe 2p and Cr 2p peaks were not detected, indicating that the steel substrate remained covered and protected by the coating during the test.

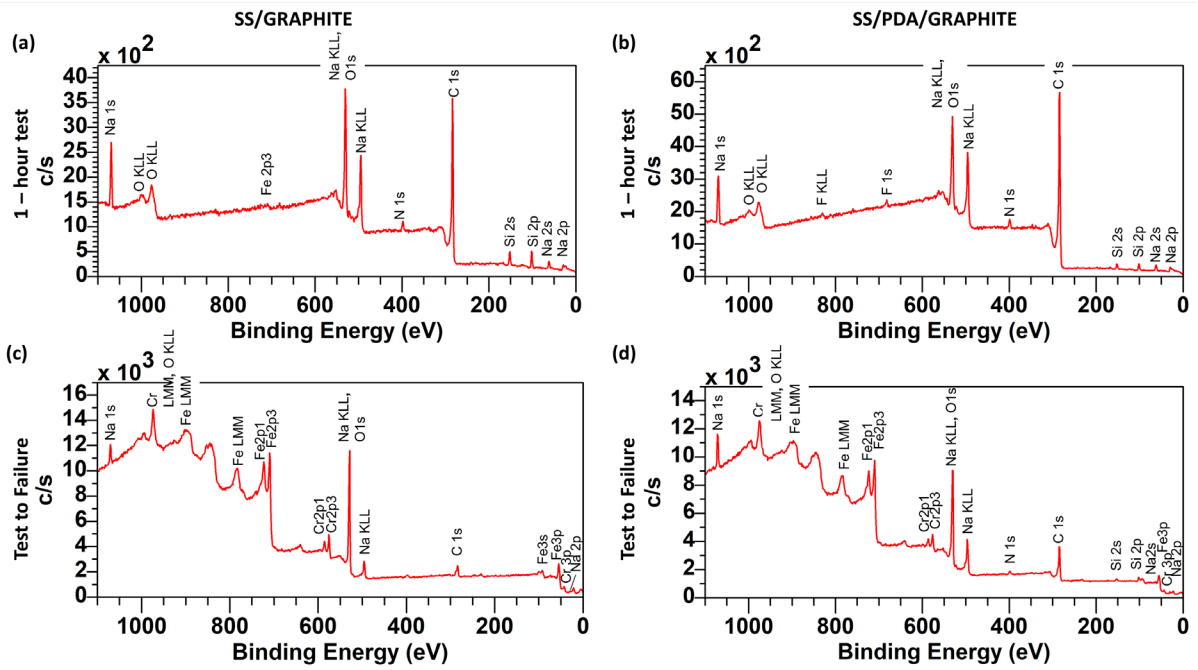


Figure 12. XPS survey spectra of worn regions after tribological testing: (**a**,**b**) coatings after 1 h sliding (no failure, COF < 0.5), and (**c**,**d**) coatings tested to failure (COF ≥ 0.5). (**a**,**c**) SS/graphite and (**b**,**d**) SS/PDA/graphite. In the 1 h condition, no Fe 2p or Cr 2p peaks were detected, confirming that the substrate remained protected. The run-to-failure condition showed strong Fe and Cr peaks, together with increased O 1s intensity, consistent with exposure of the steel substrate and oxide formation. Signals from C 1s (graphite) and Na 1s (dispersant residue) dominate both spectra.

In contrast, for samples tested to failure (Figure 12c,d), clear Fe 2p, Fe LMM, and Cr 2p peaks were present, confirming exposure of the underlying steel substrate due to coating degradation. The Cr $2p_1/_2$ and Cr $2p_3/_2$ doublets, along with increased O 1s intensity, suggest oxidation of the exposed surface, likely forming iron and chromium oxides such as Fe_2O_3, Fe_3O_4, and Cr_2O_3.

Although Fe and Cr signals were detectable via EDS after 1 h of sliding, they were absent in XPS under the same condition. This discrepancy is attributed to the difference in sampling depth: EDS probes approximately 1 μm into the material, capturing deeper substrate contributions, whereas XPS is surface-sensitive and only samples the outermost few nanometers. The lack of Fe in XPS therefore confirms that the steel remained covered by a thin graphite-rich film, even when EDS detected elements from the bulk.

No substantial differences were observed between SS/graphite and SS/PDA/graphite in the XPS survey spectra at either condition. Although PDA may introduce C–N or C–O bonding signatures, its contributions are difficult to isolate within the broader graphite-derived C 1s envelope. Nitrogen was present in both systems; however, its detection in the SS/graphite group suggests it may arise from atmospheric adsorption or processing residues rather than PDA-specific chemistry.

Overall, the XPS results demonstrate that both graphite-based coatings provided sufficient coverage to prevent substrate exposure during early sliding. Substrate elements

only became detectable after coating failure, consistent with the observed friction behavior and wear track morphology.

3.7. Summary of Wear Mechanisms

The tribological and materials characterization results demonstrate distinct wear mechanisms for graphite and PDA/graphite coatings. In graphite-only systems, poor interfacial adhesion leads to severe plowing and early coating delamination, exposing the steel substrate and triggering aggressive wear modes. Once the underlying metal is reached, sliding induces abrasive and adhesive interactions that rapidly deteriorate the surface. Detached graphite debris is displaced toward the edges of the wear track, while transfer film forms early, but tends to be thick and mechanically fragile, offering only transient protection.

In contrast, PDA/graphite coatings exhibit substantially greater wear resistance. The PDA interlayer enhances adhesion at both the substrate and interflake levels, which helps coating retention under load. During sliding, graphite is gradually compacted within the wear path, forming densified, carbon-rich zones that resist coating removal and delay substrate exposure. These compacted regions are more resistant to disruption, leading to the development of stable and cohesive transfer films on the counterface. As a result, wear is confined to localized zones, and the coatings persist significantly longer than graphite-only counterparts.

This divergence in wear behavior is driven by differences in adhesion strength and material retention, as supported by SEM and EDS observations. Despite similar low friction values, graphite alone is prone to rapid depletion, while the PDA-modified system promotes a more gradual wear process, preserving protective surface coverage and mitigating severe damage.

3.8. Broader Discussion

The combined results underscore the dual role of PDA in graphite-based coatings: it modestly increases friction but substantially extends durability. Graphite-only coatings reduce friction effectively but suffer from poor adhesion and short service life. In contrast, PDA/graphite coatings maintain a COF below 0.15 while withstanding sliding up to seven times longer.

Characterization data support this mechanistic picture. SEM and EDS reveal improved coating retention and densified regions; counterface imaging confirms more cohesive transfer films. Raman spectroscopy shows that graphitic bonding remains intact, with only minor shifts in the G-band suggesting local compaction or stress-induced reorganization. XPS further confirms that the steel substrate remains covered during early sliding, with failure marked by the appearance of Fe and Cr signals and surface oxide formation.

These findings are consistent with trends in solid lubricant design, where transfer-film cohesion and interfacial adhesion strongly influence longevity. The slight friction tradeoff introduced by PDA is well within the performance range of graphite and compares favorably with other solid lubricants such as h-BN or MoS_2 [42]. Optimizing PDA thickness and deposition conditions may help fine-tune the balance between friction and durability. Future evaluation of processing cost and scalability will further increase industrial relevance.

Overall, PDA functions as both a molecular adhesive and a structural stabilizer, offering a practical route to extend the lifetime and reliability of carbon-based tribological coatings.

4. Conclusions

This study demonstrates that incorporating PDA as an interlayer significantly improves the tribological performance of graphite coatings under dry sliding. Compared to graphite-only systems, PDA/graphite coatings maintained a low COF below 0.15 and extended sliding lifetime by over sevenfold. Mechanistically, PDA improved adhesion at the coating-substrate interface, leading to reduced material loss, delayed substrate exposure, and confined wear damage. This transition from abrasive to compression-dominated wear was confirmed by SEM, profilometry, and counterface imaging. Spectroscopic analyses further support these conclusions. Raman spectra revealed minimal disruption to graphitic bonding and slight G-band shifts consistent with compaction. XPS confirmed that substrate exposure was prevented under 1 h sliding wear conditions and correlated with Fe and Cr signals only after failure. Together, these results highlight PDA's role in stabilizing tribofilms and promoting long-term graphite coating integrity under high contact pressure. This approach offers a promising strategy for enhancing the durability of solid lubricants in applications where extended wear resistance and low friction are critical.

Supplementary Materials: The following supporting information can be downloaded at: https://www.mdpi.com/article/10.3390/lubricants13100433/s1, Figure S1: EDS spectrum, SEM and elemental maps of (a) SS/graphite and (b) SS/PDA/graphite wear tracks after 1-hour of sliding. Figure S2: EDS spectrum, SEM and elemental maps of (a) SS/graphite and (b) SS/PDA/graphite wear tracks after coating failure.

Author Contributions: Conceptualization, A.A. and M.Z.; methodology, A.A.; investigation, A.A., F.M.d.O., D.O. and M.B.; data curation, A.A.; formal analysis, A.A.; resources, M.Z., Y.I.M. and J.C.; writing—original draft, A.A.; writing—review and editing, A.A., F.M.d.O., D.O., M.B., J.C., Y.I.M. and M.Z.; visualization, A.A.; supervision, M.Z.; project administration, M.Z.; funding acquisition, M.Z. All authors have read and agreed to the published version of the manuscript.

Funding: This research was funded by the National Science Foundation under Grant Award # 2141026.

Data Availability Statement: The original contributions presented in the study are included in the article, further inquiries can be directed to the corresponding author.

Acknowledgments: This work was supported by the National Science Foundation under Grant Award # 2141026. Any opinions, findings, and conclusions or recommendations expressed in this material are those of the authors and do not necessarily reflect the views of the National Science Foundation. We acknowledge AML Industries for providing the aqueous graphite dispersion. The Materials Characterization Facility at the University of Arkansas was used to obtain SEM, EDS, and XPS data.

Conflicts of Interest: The authors declare no conflicts of interest.

References

1. Scharf, T.W.; Prasad, S.V. Solid lubricants: A review. *J. Mater. Sci.* **2013**, *48*, 511–531. [CrossRef]
2. Ayyagari, A.V.; Mutyala, K.C.; Sumant, A.V. Towards developing robust solid lubricant operable in multifarious environments. *Sci. Rep.* **2020**, *10*, 15390. [CrossRef] [PubMed]
3. Berman, D.; Erdemir, A.; Sumant, A.V. Graphene: A new emerging lubricant. *Mater. Today* **2014**, *17*, 31–42. [CrossRef]
4. Kumar, R.; Hussainova, I.; Rahmani, R.; Antonov, M. Solid Lubrication at High-Temperatures—A Review. *Materials* **2022**, *15*, 1695. [CrossRef]
5. Torres, H.; Podgornik, B.; Jovičević-Klug, M.; Rodríguez Ripoll, M. Compatibility of graphite, hBN and graphene with self-lubricating coatings and tool steel for high temperature aluminium forming. *Wear* **2022**, *490–491*, 204187. [CrossRef]
6. Podgornik, B.; Kosec, T.; Kocijan, A.; Donik. Tribological behaviour and lubrication performance of hexagonal boron nitride (h-BN) as a replacement for graphite in aluminium forming. *Tribol. Int.* **2015**, *81*, 267–275. [CrossRef]

7. Rahman, M.M.; Islam, M.; Roy, R.; Younis, H.; AlNahyan, M.; Younes, H. Carbon Nanomaterial-Based Lubricants: Review of Recent Developments. *Lubricants* **2022**, *10*, 281. [CrossRef]
8. Ouyang, J.H.; Li, Y.F.; Zhang, Y.Z.; Wang, Y.M.; Wang, Y.J. High-Temperature Solid Lubricants and Self-Lubricating Composites: A Critical Review. *Lubricants* **2022**, *10*, 177. [CrossRef]
9. Wang, Z.; Fu, Q.; Wu, S. Effect of solid lubricant particles on the tribological properties of PTFE composites lubricated with natural seawater. *J. Dispers. Sci. Technol.* **2019**, *40*, 239–249. [CrossRef]
10. Ye, S.; Zeng, X. Tribological properties of PTFE and PTFE composites at different temperatures. *Tribol. Lubr. Technol.* **2014**, *70*, 32–39. [CrossRef]
11. Wang, R.; Zhang, F.; Yang, K.; Xiao, N.; Tang, J.; Xiong, Y.; Zhang, G.; Duan, M.; Chen, H. Important contributions of carbon materials in tribology: From lubrication abilities to wear mechanisms. *J. Alloys Compd.* **2024**, *979*, 173454. [CrossRef]
12. Marcinauskas, L.; Mathew, J.S.; Milieška, M.; Aikas, M.; Kalin, M. Effect of graphite concentration on the tribological performance of alumina coatings. *J. Alloys Compd.* **2020**, *827*, 154135. [CrossRef]
13. Ye, W.; Shi, Y.; Zhou, Q.; Xie, M.; Wang, H.; Bou-Saïd, B.; Liu, W. Recent advances in self-lubricating metal matrix nanocomposites reinforced by carbonous materials: A review. *Nano Mater. Sci.* **2024**, *6*, 701–713. [CrossRef]
14. Ren, Y.; Zhang, L.; Xie, G.; Li, Z.; Chen, H.; Gong, H.; Xu, W.; Guo, D.; Luo, J. A review on tribology of polymer composite coatings. *Friction* **2021**, *9*, 429–470. [CrossRef]
15. Wu, H.; Zhang, H.; Gao, A.; Gong, L.; Ji, Y.; Zeng, S.; Li, S.; Wang, X. Friction and wear performance of aluminum-based self-lubricating materials derived from the 3D printed graphite skeletons with different morphologies and orientations. *Tribol. Int.* **2024**, *195*, 109614. [CrossRef]
16. Choudhury, D.; Niyonshuti, I.I.; Chen, J.; Goss, J.A.; Zou, M. Tribological performance of polydopamine + Ag nanoparticles/PTFE thin films. *Tribol. Int.* **2020**, *144*, 106097. [CrossRef]
17. Pan, G.; Guo, Q.; Ding, J.; Zhang, W.; Wang, X. Tribological behaviors of graphite/epoxy two-phase composite coatings. *Tribol. Int.* **2010**, *43*, 1318–1325. [CrossRef]
18. Morstein, C.E.; Dienwiebel, M. Graphite lubrication mechanisms under high mechanical load. *Wear* **2021**, *477*, 203794. [CrossRef]
19. Al-Asadi, M.M.; Al-Tameemi, H.A. A review of tribological properties and deposition methods for selected hard protective coatings. *Tribol. Int.* **2022**, *176*, 107919. [CrossRef]
20. Abe, A.; Zou, M. Enhanced Scratch Resistance of Graphite Coating Using a Polydopamine Adhesive Underlayer. *Coatings* **2025**, *15*, 690. [CrossRef]
21. Tran, N.T.; Flanagan, D.P.; Orlicki, J.A.; Lenhart, J.L.; Proctor, K.L.; Knorr, D.B. Polydopamine and Polydopamine-Silane Hybrid Surface Treatments in Structural Adhesive Applications. *Langmuir* **2018**, *34*, 1274–1286. [CrossRef] [PubMed]
22. Beckford, S.; Zou, M. Wear resistant PTFE thin film enabled by a polydopamine adhesive layer. *Appl. Surf. Sci.* **2014**, *292*, 350–356. [CrossRef]
23. Liu, Y.; Ai, K.; Lu, L. Polydopamine and its derivative materials: Synthesis and promising applications in energy, environmental, and biomedical fields. *Chem. Rev.* **2014**, *114*, 5057–5115. [CrossRef] [PubMed]
24. Ryu, J.; Ku, S.H.; Lee, H.; Park, C.B. Mussel-inspired polydopamine coating as a universal route to hydroxyapatite crystallization. *Adv. Funct. Mater.* **2010**, *20*, 2132–2139. [CrossRef]
25. Zhang, M.; Mi, M.; Hu, Z.; Li, L.; Chen, Z.; Gao, X.; Liu, D.; Xu, B.; Liu, Y. Polydopamine-Based Biomaterials in Orthopedic Therapeutics: Properties, Applications, and Future Perspectives. *Drug Des. Dev. Ther.* **2024**, *18*, 3765–3790. [CrossRef]
26. Guo, S.; Pang, C.; He, P.; He, X.; Ren, J.; Ouyang, L. Effective coating of polydopamine-mediated polyacrylamide on SiOx microparticles enables stable interface chemistry. *Appl. Surf. Sci.* **2024**, *651*, 159255. [CrossRef]
27. Haidar, D.R.; Ye, J.; Moore, A.C.; Burris, D.L. Assessing quantitative metrics of transfer film quality as indictors of polymer wear performance. *Wear* **2017**, *380–381*, 78–85. [CrossRef]
28. Ge, X.; Chai, Z.; Shi, Q.; Liu, Y.; Wang, W. Graphene superlubricity: A review. *Friction* **2023**, *11*, 1953–1973. [CrossRef]
29. Tomanik, E.; Christinelli, W.; Souza, R.M.; Oliveira, V.L.; Ferreira, F.; Zhmud, B. Review of Graphene-Based Materials for Tribological Engineering Applications. *Eng* **2023**, *4*, 2764–2811. [CrossRef]
30. Buzio, R.; Gerbi, A.; Bernini, C.; Repetto, L.; Vanossi, A. Graphite superlubricity enabled by triboinduced nanocontacts. *Carbon* **2021**, *184*, 875–890. [CrossRef]
31. Qu, C.; Wang, K.; Wang, J.; Gongyang, Y.; Carpick, R.W.; Urbakh, M.; Zheng, Q. Origin of friction in superlubric graphite contacts. *Phys. Rev. Lett.* **2020**, *125*, 126102. [CrossRef]
32. Jiang, Y.; Choudhury, D.; Brownell, M.; Nair, A.; Goss, J.A.; Zou, M. The effects of annealing conditions on the wear of PDA/PTFE coatings. *Appl. Surf. Sci.* **2019**, *481*, 723–735. [CrossRef]
33. Zhao, Y.; Zou, M. Experimental investigation of the wear mechanisms of thin PDA/PTFE coatings. *Prog. Org. Coat.* **2019**, *137*, 105341. [CrossRef]

34. Zhou, P.; Deng, Y.; Lyu, B.; Zhang, R.; Zhang, H.; Ma, H.; Lyu, Y.; Wei, S. Rapidly-deposited polydopamine coating via high temperature and vigorous stirring: Formation, characterization and biofunctional evaluation. *PLoS ONE* **2014**, *9*, e113087. [CrossRef]
35. Ryu, J.H.; Messersmith, P.B.; Lee, H. Polydopamine Surface Chemistry: A Decade of Discovery. *ACS Appl. Mater. Interfaces* **2018**, *10*, 7523–7540. [CrossRef]
36. Ferrari, A.C.; Robertson, J. Interpretation of Raman spectra of disordered and amorphous carbon. *Phys. Rev. B* **2000**, *61*, 14095–14107. [CrossRef]
37. Lan, Y.; Zondode, M.; Deng, H.; Yan, J.A.; Ndaw, M.; Lisfi, A.; Wang, C.; Pan, Y.-L. Basic concepts and recent advances of crystallographic orientation determination of graphene by raman spectroscopy. *Crystals* **2018**, *8*, 375. [CrossRef]
38. Ferrari, A.C. Raman spectroscopy of graphene and graphite: Disorder, electron-phonon coupling, doping and nonadiabatic effects. *Solid State Commun.* **2007**, *143*, 47–57. [CrossRef]
39. Chen, G.; Zhao, J.; Chen, K.; Liu, S.; Zhang, M.; He, Y.; Luo, J. Ultrastable lubricating properties of robust self-repairing tribofilms enabled by in situ-assembled polydopamine nanoparticles. *Langmuir* **2020**, *36*, 852–861. [CrossRef]
40. Zhang, W.; Yang, F.K.; Han, Y.; Gaikwad, R.; Leonenko, Z.; Zhao, B. Surface and tribological behaviors of the bioinspired polydopamine thin films under dry and wet conditions. *Biomacromolecules* **2013**, *14*, 394–405. [CrossRef] [PubMed]
41. Ball, V.; Del Frari, D.; Michel, M.; Buehler, M.J.; Toniazzo, V.; Singh, M.K.; Gracio, J.; Ruch, D. Deposition Mechanism and Properties of Thin Polydopamine Films for High Added Value Applications in Surface Science at the Nanoscale. *BioNanoScience* **2011**, *2*, 16–34. [CrossRef]
42. Vergari, L.; Quincey, J.; Meric de Bellefon, G.; Merriman, T.; Hackett, M.; Scarlat, R.O. Self-lubrication of nuclear graphite in argon at high temperature. *Tribol. Int.* **2023**, *177*, 107946. [CrossRef]
43. Goyal, R.K.; Yadav, M. The Wear and Friction Behavior of Novel Polytetrafluoroethylene/Expanded Graphite Nanocomposites for Tribology Application. *J. Tribol.* **2013**, *136*, 021601. [CrossRef]
44. Dienwiebel, M.; Pradeep, N.; Verhoeven, G.S.; Zandbergen, H.W.; Frenken, J.W.M. Model experiments of superlubricity of graphite. *Surf. Sci.* **2005**, *576*, 197–211. [CrossRef]
45. Morstein, C.E.; Klemenz, A.; Dienwiebel, M.; Moseler, M. Humidity-dependent lubrication of highly loaded contacts by graphite and a structural transition to turbostratic carbon. *Nat. Commun.* **2022**, *13*, 5958. [CrossRef]
46. Scheidt, H.A.; Filip, C.; Turcu, R.; Bende, A.; Beck, S. Structure of Polydopamine: A Never-Ending Story? *Langmuir* **2013**, *29*, 10539–10548. [CrossRef] [PubMed]
47. Kim, Y.; Kim, J. Carbonization of polydopamine-coating layers on boron nitride for thermal conductivity enhancement in hybrid polyvinyl alcohol (PVA) composites. *Polymers* **2020**, *12*, 1410. [CrossRef] [PubMed]
48. Seo, J.; Hyun, S.; Moon, J.; Yeong Lee, J.; Kim, C. High Performance of a Polydopamine-Coated Graphite Anode with a Stable SEI Layer. *ACS Appl. Energy Mater.* **2022**, *5*, 5610–5616. [CrossRef]
49. Cortés, M.T.; Vargas, C.; Blanco, D.A.; Quinchanegua, I.D.; Cortés, C.; Jaramillo, A.M. Bioinspired Polydopamine Synthesis and Its Electrochemical Characterization. *J. Chem. Educ.* **2019**, *96*, 1250–1255. [CrossRef]
50. Wang, D.D.; Gao, X.; Zhao, L.; Zhou, J.; Zhuo, S.; Yan, Z.; Xing, W. Polydopamine-coated graphene nanosheets as efficient electrocatalysts for oxygen reduction reaction. *RSC Adv.* **2018**, *8*, 16044–16051. [CrossRef]
51. Yan, Q.; Xu, L.; Zhao, Y.; Wu, F.; Chen, R.; Li, L. Regenerated Graphite-Derived Cellular-Inspired Polydopamine@NiO@Graphite toward Robust Lithium Storage. *ACS Appl. Mater. Interfaces* **2023**, *15*, 25506–25515. [CrossRef]

Disclaimer/Publisher's Note: The statements, opinions and data contained in all publications are solely those of the individual author(s) and contributor(s) and not of MDPI and/or the editor(s). MDPI and/or the editor(s) disclaim responsibility for any injury to people or property resulting from any ideas, methods, instructions or products referred to in the content.